

PAPER • OPEN ACCESS

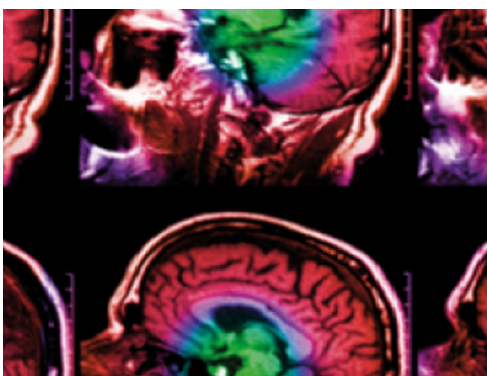
In silico evaluation and optimisation of magnetic resonance elastography of the liver

To cite this article: Deirdre M McGrath *et al* 2021 *Phys. Med. Biol.* **66** 225005

View the [article online](#) for updates and enhancements.

You may also like

- [The features of band structures for woodpile three-dimensional photonic crystals with plasma and function dielectric constituents](#)
Haifeng ZHANG, , Hao ZHANG *et al.*
- [Commuting quantum circuits and complexity of Ising partition functions](#)
Keisuke Fujii and Tomoyuki Morimae
- [Verifying commuting quantum computations via fidelity estimation of weighted graph states](#)
Masahito Hayashi and Yuki Takeuchi



IPEM | IOP

Series in Physics and Engineering in Medicine and Biology

Your publishing choice in medical physics,
biomedical engineering and related subjects.

Start exploring the collection—download the
first chapter of every title for free.



PAPER

In silico evaluation and optimisation of magnetic resonance elastography of the liver

OPEN ACCESS

RECEIVED
12 May 2021REVISED
7 September 2021ACCEPTED FOR PUBLICATION
22 October 2021PUBLISHED
10 November 2021

Original content from this work may be used under the terms of the [Creative Commons Attribution 4.0 licence](https://creativecommons.org/licenses/by/4.0/).

Any further distribution of this work must maintain attribution to the author(s) and the title of the work, journal citation and DOI.

Deirdre M McGrath^{1,2} , Christopher R Bradley^{1,2}  and Susan T Francis^{1,2} ¹ Sir Peter Mansfield Imaging Centre, University of Nottingham, University Park, Nottingham NG7 2RD, United Kingdom² NIHR Nottingham Biomedical Research Centre, Radiological Sciences, Division of Clinical Neuroscience, Queens Medical Centre, Nottingham, NG7 2UH, United KingdomE-mail: Deirdre.McGrath@nottingham.ac.uk**Keywords:** magnetic resonance elastography, simulation, finite element modelling, liver, fibrosis, cirrhosisSupplementary material for this article is available [online](#)

Abstract

Objective. Magnetic resonance elastography (MRE) is widely adopted as a biomarker of liver fibrosis. However, *in vivo* MRE accuracy is difficult to assess. **Approach.** Finite element model (FEM) simulation was employed to evaluate liver MRE accuracy and inform methodological optimisation. MRE data was simulated in a 3D FEM of the human torso including the liver, and compared with spin-echo echo-planar imaging MRE acquisitions. The simulated MRE results were compared with the ground truth magnitude of the complex shear modulus ($|G^*|$) for varying: (1) ground truth liver $|G^*|$; (2) simulated imaging resolution; (3) added noise; (4) data smoothing. Motion and strain-based signal-to-noise (SNR) metrics were evaluated on the simulated data as a means to select higher-quality voxels for preparation of acquired MRE summary statistics of $|G^*|$. **Main results.** The simulated MRE accuracy for a given ground truth $|G^*|$ was found to be a function of imaging resolution, motion-SNR and smoothing. At typical imaging resolutions, it was found that due to under-sampling of the MRE wave-field, combined with motion-related noise, the reconstructed simulated $|G^*|$ could contain errors on the scale of the difference between liver fibrosis stages, e.g. 54% error for ground truth $|G^*| = 1$ kPa. Optimum imaging resolutions were identified for given ground truth $|G^*|$ and motion-SNR levels. **Significance.** This study provides important knowledge on the accuracy and optimisation of liver MRE. For example, for motion-SNR ≤ 5 , to distinguish between liver $|G^*|$ of 2 and 3 kPa (i.e. early-stage liver fibrosis) it was predicted that the optimum isotropic voxel size is 4–6 mm.

1. Introduction

Magnetic resonance elastography (MRE) (McGrath 2018) is a powerful diagnostic tool to determine the biomechanical properties of biological tissue. Through its sensitivity to pathology-driven changes in tissue biomechanics, MRE can detect disease such as fibrosis (Yin *et al* 2007, Singh *et al* 2015). There are two broad classes of MRE, dynamic (Muthupillai *et al* 1995) and static (or ‘quasi-static’) methods (McGrath *et al* 2012). In the former, mechanical waves are delivered, while the latter involves applying a compressive force to the whole tissue volume. For both, the resulting displacement field is measured using motion encoding gradients (MEGs) and the biomechanical properties are estimated from the measurements using an inversion algorithm to produce an ‘elastogram’. Dynamic MRE has been widely adopted for the detection and staging of hepatic fibrosis and cirrhosis (Singh *et al* 2015, Mathew and Venkatesh 2018). However, a number of questions remain with regard to MRE validation.

Crucially, it is difficult to determine the true accuracy of clinical MRE. Comparison with mechanical bench-top testing of surgically-resected tissue is usually not possible in human studies. Biopsy cores can be removed to assess liver fibrosis via histological analysis (Morisaka *et al* 2018). However, the biomechanical properties of

ex vivo tissue do not match the *in vivo* state due to loss of hydration and blood pressure, removal from the tissue matrix, and potential damage and loss of structural integrity.

Commonly physical phantoms are built to test MRE and benchmark accuracy. However it is difficult to make anthropomorphic phantoms that reproduce the *in vivo* MRE motion field; although some work has been done on breast phantoms (Madsen *et al* 1988, Madsen *et al* 2006). In liver MRE, the vibrations delivered to the skin undergo multiple reflections and refractions at anatomical interfaces, e.g. the ribs. Hence, the *in vivo* wave pattern is more complex than that of a geometric and homogeneous phantom, and an inversion algorithm that performs well for a phantom will not necessarily be optimal for *in vivo* tissue. Furthermore, the ground truth mechanical properties of the phantom material might be difficult to determine. For water-based materials, e.g. gelatine, the properties may be temperature-dependent, or change over time with dehydration. Moreover, non-water-based materials, e.g. acrylics, might not include sufficient viscosity to model biological tissue.

The determination of *in vivo* MRE accuracy is challenging, as it is influenced by multiple factors. One solution is to validate MRE methods using computational modelling, as demonstrated for brain (McGrath *et al* 2016, McGrath *et al* 2017). The advantage of this approach is that the ground truth mechanical properties are known *a priori* and can be compared with the inversion-reconstructed properties to measure accuracy. Anthropomorphic *in silico* models can be generated from anatomical imaging data and used to simulate MRE motion fields in the body. The computed data can be compared with MRE data measured from the same individual, to evaluate the realism of the simulation. Further, *in silico* data can be used to validate and optimise MRE acquisition methodology and inversion algorithms.

This work presents finite element model (FEM) based MRE simulations to optimise MRE acquisitions and assess the accuracy of MRE to measure liver biomechanical properties. The purpose of this initial study is to investigate the potential of simulation-based MRE evaluation, starting with the model of a healthy individual; while future studies with models of other volunteers and patients will be needed to fully examine this technique. It should be recognised that the realism of simulations is necessarily limited in various aspects, which might influence the accuracy of absolute simulated values. But such simulations do allow the exploration of the sensitivity of MRE to detect a change in mechanical properties with disease, to assess the linearity of MRE measures with respect to underlying properties and the potential influence of factors such as imaging resolution.

Recent research has reported the advantages of spin-echo echo-planar imaging (SE-EPI) MRE over gradient-echo based MRE methods for the liver, in particular for 3 Tesla (T) where magnetic field inhomogeneity effects are pronounced in patients with high liver iron load and thus short transverse relaxation time (T_2^*) (Cunha *et al* 2018). Therefore SE-EPI MRE was acquired and compared with the simulated MRE in the same individual whose data was simulated.

2. Materials and methods

2.1. MRI acquisitions

MRI data was collected on a 3-T Philips Ingenia scanner (Philips Medical Systems, Best, Netherlands), with MRE implemented using the Resoundant acoustic wave delivery system (Resoundant Inc., Rochester, MN) (Venkatesh *et al* 2013). Calculations and image processing were carried out in MATLAB (R2017b, MathWorks Inc., Natick, Massachusetts, USA).

One healthy male volunteer (age 26 years) was scanned with informed consent and in accordance with local research ethics guidance.

In MRE, multiple acquisitions capture the wave field at different snap-shots in time. These are combined via discrete Fourier transform (DFT) to obtain a harmonic steady-state complex displacement field, \mathbf{u}

$$u(\mathbf{x}, t) = u(\mathbf{x}) \exp(i\omega t), \quad (1)$$

where ω is the angular frequency of the vibration. Time-steps are collected by varying the phase offset (α) between the mechanical wave and the MEG. In this study the number of phase offsets (N_{PO}) was set to 8, i.e. 8 values of α between 0 and 2π .

Four SE-EPI MRE acquisitions were made with different isotropic spatial resolutions and driver frequencies using the scan parameters: (1) Voxel dimension = $4 \times 4 \times 4 \text{ mm}^3$, Frequency (freq) = 60 Hz, field of view (FOV) = $384 \times 384 \times 24 \text{ mm}^3$, matrix = $96 \times 96 \times 6$, repetition time (TR) = 600 ms, echo time (TE) = 58 ms, EPI factor = 39; (2) Voxel dimension = $5 \times 5 \times 5 \text{ mm}^3$, freq = 60 Hz, FOV = $400 \times 400 \times 30 \text{ mm}^3$; matrix = $80 \times 80 \times 6$, TR = 600 ms, TE = 58 ms, EPI factor = 33; (3) Voxel dimension = $6 \times 6 \times 6 \text{ mm}^3$, freq = 60 Hz, FOV = $384 \times 384 \times 36 \text{ mm}^3$; matrix = $64 \times 64 \times 6$, TR = 600 ms, TE = 58 ms, EPI factor = 27; (4) Voxel dimension = $6 \times 6 \times 6 \text{ mm}^3$, freq = 50 Hz, FOV = $384 \times 384 \times 36 \text{ mm}^3$; matrix = $64 \times 64 \times 6$, TR = 720 ms, TE = 70 ms, EPI factor = 27. One signal average was employed throughout. Each scan duration was 16 s, in which 8 phase offsets were collected during an end-expiration

breath-hold. In each acquisition six axial slices covering the central liver volume were collected. Voxel sizes were chosen based on the simulation results for healthy liver. The frequency was changed to explore variability in the degree of wave attenuation.

MRE acquisitions were repeated to collect each of the MEG directions (head-foot (H-F), anterior–posterior (A-P), right-left (R-L)), with the motion of the tissue in the direction of the applied MEG encoded as phase-shifts which are directly proportional to the displacements. Separate acquisitions confirmed the volunteer had T_2^*/T_2 values within a healthy liver range (Kritsaneeapaiboon *et al* 2018).

For FEM preparation, a whole-body anatomical imaging was collected on the same subject using a multi-point gradient-echo based Dixon (mDixon) scan (Dixon 1984, Xiang 2006) using the scan parameters: FOV = $448 \times 560 \times 300 \text{ mm}^3$, matrix = $280 \times 280 \times 200$, voxel = $1 \times 1 \times 1.5 \text{ mm}^3$; TR = 3 ms, TE = 1.12 and 1.99 ms, flip angle = 10° , signal averages = 1. The mDixon method was chosen as it provided a variety of contrasts to inform the data segmentation for the FEM: water-only, fat-only and in-phase and opposed-phase images.

2.2. Calculation of motion- and strain-based SNR to evaluate MRE accuracy

An aim of this study was to explore potential metrics for selection of higher-quality elastogram data, and both motion- and strain-based SNR were considered. Motion-based SNR is likely to be more informative than imaging-SNR; where the measured motion is proportional to the phase-shift accrued by the tissue moving in the MEG.

The DFT of measured displacements obtaining the harmonic steady-state can be described as fitting a sinusoid S to each voxel of the data (for each motion direction):

$$S = \text{Re}\{ue^{i\omega t}\}, \quad (2)$$

where u is the complex-valued amplitude for the voxel in a given direction. In McGarry *et al* (2011), the noise of the measured displacements N_{meas} was estimated as the standard deviation (SD) of differences between measured and fitted displacements:

$$N_{meas} = \sigma\{d_i - u \cos(\omega t_i)\}, \quad (3)$$

where σ indicates the SD over the phase offsets and d_i represents the measured displacements at the different phase offset time-steps t_i ($\omega t_i \equiv \alpha_i$). The noise of the fitted displacement amplitude N_{amp} was related to N_{meas} via the propagation of uncertainties through the DFT (McGarry *et al* 2011):

$$N_{amp} = \sqrt{\frac{2}{N_{PO}}} N_{meas}. \quad (4)$$

The SNR based on the measured displacements divided by N_{meas} is referred to as MM-SNR ('measured-motion' SNR), and that based on the real component of the steady-state amplitudes and N_{amp} is denoted MA-SNR ('motion-amplitude' SNR). Voxel-wise MA-SNR was calculated separately for the 3 motion directions and subsequently averaged over the directions.

As the focus here is to estimate shear elastic modulus, shear strain is likely to be a more pertinent quantity than tissue displacement, which may be dominated by bulk motion. Thus octahedral shear strain (OSS) was calculated (McGarry *et al* 2011). The deviatoric or shear strain component of the OSS is:

$$\epsilon_s = \frac{2}{3} \sqrt{(\epsilon_{xx} - \epsilon_{yy})^2 + (\epsilon_{xx} - \epsilon_{zz})^2 + (\epsilon_{yy} - \epsilon_{zz})^2 + 6(\epsilon_{xy}^2 + \epsilon_{xz}^2 + \epsilon_{yz}^2)}, \quad (5)$$

where ϵ_{xx} are unique components of strain in three directions (x , y and z).

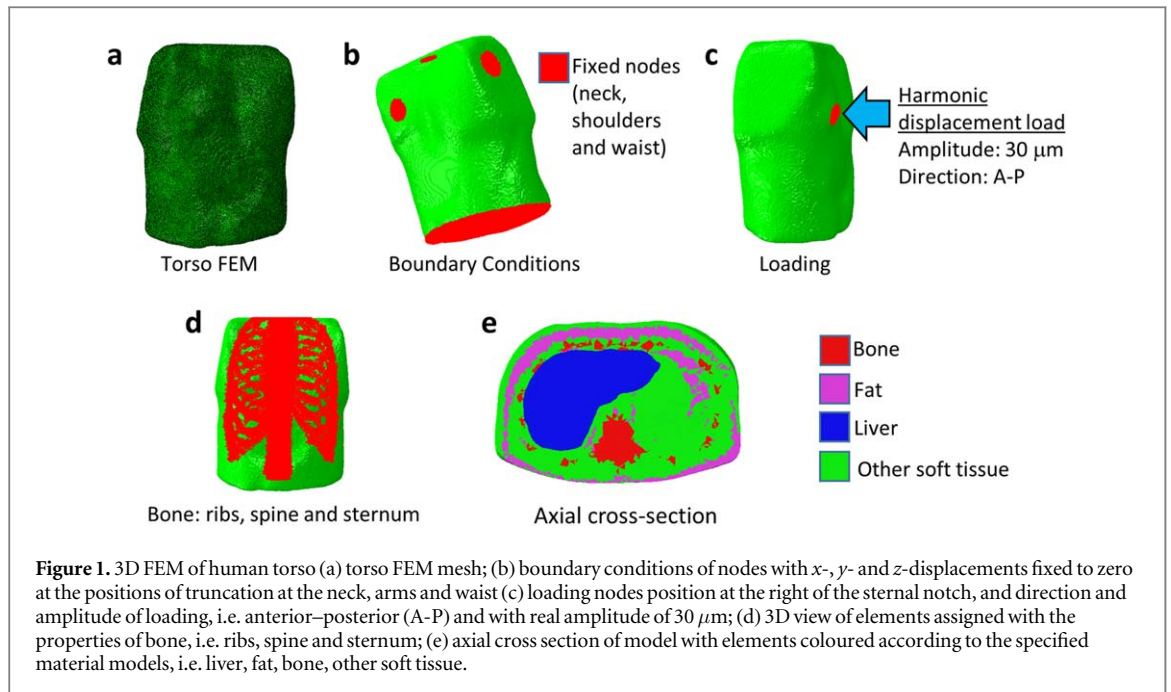
Similar to McGarry *et al* (2011), the strain noise $\epsilon_s^{\text{noise}}$ was calculated by evaluating equation (5) with strain values calculated from N_{amp} for each direction x , y , z , and SNR based on the OSS:

$$\text{OSS-SNR} = \frac{\bar{\epsilon}_s}{\epsilon_s^{\text{noise}}}, \quad (6)$$

where $\bar{\epsilon}_s$ indicates time averaging over the phase offsets. As N_{amp} is positive, a random sign was assigned to the N_{amp} values to generate a realistic noise distribution prior to calculation of $\epsilon_s^{\text{noise}}$, as used in McGarry *et al* (2011). However, while in McGarry *et al* (2011) $\bar{\epsilon}_s$ was also averaged over a volume, in this work the OSS-SNR was calculated for individual voxels, thus allowing visualisation of the spatial distribution of the OSS-SNR.

2.3. Direct Inversion to calculate MRE elastograms

For a viscoelastic material with the assumption of isotropy and local homogeneity of the material properties, solving the Navier–Stokes equation for the propagation of an acoustic wave yields the viscoelastic moduli from the motion field (Sinkus *et al* 2005). Substituting the time harmonic curl of the motion field ($\mathbf{v} = \nabla \times \mathbf{u}$) into the viscoelastic wave equation gives the Helmholtz equation:



$$-\rho\omega^2\mathbf{v} = (G' + iG'')\nabla^2\mathbf{v}, \quad (7)$$

where ρ is the material density, $\nabla^2\mathbf{v}$ is the Laplacian of the curl (Sinkus *et al* 2005), and G' and G'' are the storage and loss moduli describing the shear elasticity and viscosity respectively, which are the real and imaginary components of the complex shear modulus, G^* . In this study, the direct inversion approach of Sinkus *et al* 2005 is employed. The curl and Laplacian were calculated via finite differences, and G' and G'' solved by ‘direct inversion’ of equation (7) via a least-squares calculation. In this study G' and G'' were calculated for each voxel, from which $|G^*|$ was calculated, and the accuracy of $|G^*|$ compared with ground truth was reported.

In MRE, motion is encoded in the phase of the MR signal, which must be unwrapped and scaled by the appropriate motion-encoding scaling factor to obtain the underlying displacements (Muthupillai *et al* 1996). Alternatively, when direct inversion is employed it is not necessary to convert the phase-shifts into displacements, as the motion-encoding factor cancels out. For the acquired MRE data in this study, Laplacian phase unwrapping was employed (Dittmann *et al* 2016) prior to calculation of the steady-state harmonic phase values via DFT.

Previous MRE studies have reported that pre-filtering or smoothing of the data results in better visual appearance of the elastograms (Murphy *et al* 2013, Barnhill *et al* 2018). However, it is not clear what impact this has on accuracy. Spatial smoothing of the curl with a $3 \times 3 \times 3$ box filter was found to give optimum results in previous work (McGrath *et al* 2016) and hence this smoothing was explored for the simulated and acquired data.

Many other inversion methods have been developed for elasticity imaging (Dooley, 2012), including local frequency estimation (LFE) (Manduca *et al* 2001), iterative optimisation, such as the over-lapping subzone method (Van Houten *et al* 1999), and multi-frequency methods (Tzschätzsch *et al* 2016).

In order to provide a comparison with direct inversion, the LFE algorithm (MREWave, Mayo Clinic, www.mayo.edu/research/documents/mrewave) was also applied to the acquired MRE data and the simulated data with no added noise (see supplementary information). Three motion directions were incorporated and filtering was explored.

2.4. Simulation of liver MRE using an anthropomorphic phantom of the torso

Simulation of MRE was carried out using Abaqus 2017 (Dassault Systèmes Simulia Corp, Johnston, Rhode Island, USA), and used direct-solution steady-state dynamic analysis: a perturbation procedure for which the model response to an applied harmonic vibration is calculated about a base state, generating complex frequency-space steady-state nodal displacements \mathbf{u} (equation (1)).

An anthropomorphic FEM of the torso was generated, consisting of sub-regions: liver, bone, fat and generalised soft tissue (figure 1). The bone region consisted of ribs, spine and sternum (figure 1(d)), and the fat included subcutaneous and visceral fat (figure 1(e)). The addition of bone and fat introduced material heterogeneity to enhance the realism of the model, and in particular the ribs and spine were added to simulate wave reflection and scattering effects. In MRE the compression wave delivered at the skin is partially mode-

Table 1. Modelled tissue material properties in torso FEM.

Tissue type	Frequency (Hz)	G' (kPa)	G''(kPa)	G* (kPa)	Poisson's ratio	Density (kg m ⁻³)	Shear wavelength (mm)
Liver - LM1	60	0.6	0.8	1.0	0.499	1000	13
Liver - LM2	60	1.833	0.8	2.0	0.499	1000	23
Liver - LM3	60	2.891	0.8	3.0	0.499	1000	28
Liver - LM4	60	3.919	0.8	4.0	0.499	1000	33
Liver - LM5	60	4.936	0.8	5.0	0.499	1000	37
Fat	60	0.95	0.32	1.0	0.499	1000	16
Soft tissue	60	4.5	2.2	5.0	0.499	1000	35
		Young's Modulus <i>E</i> (MPa)					
Bone	60	10			0.25	1830	779

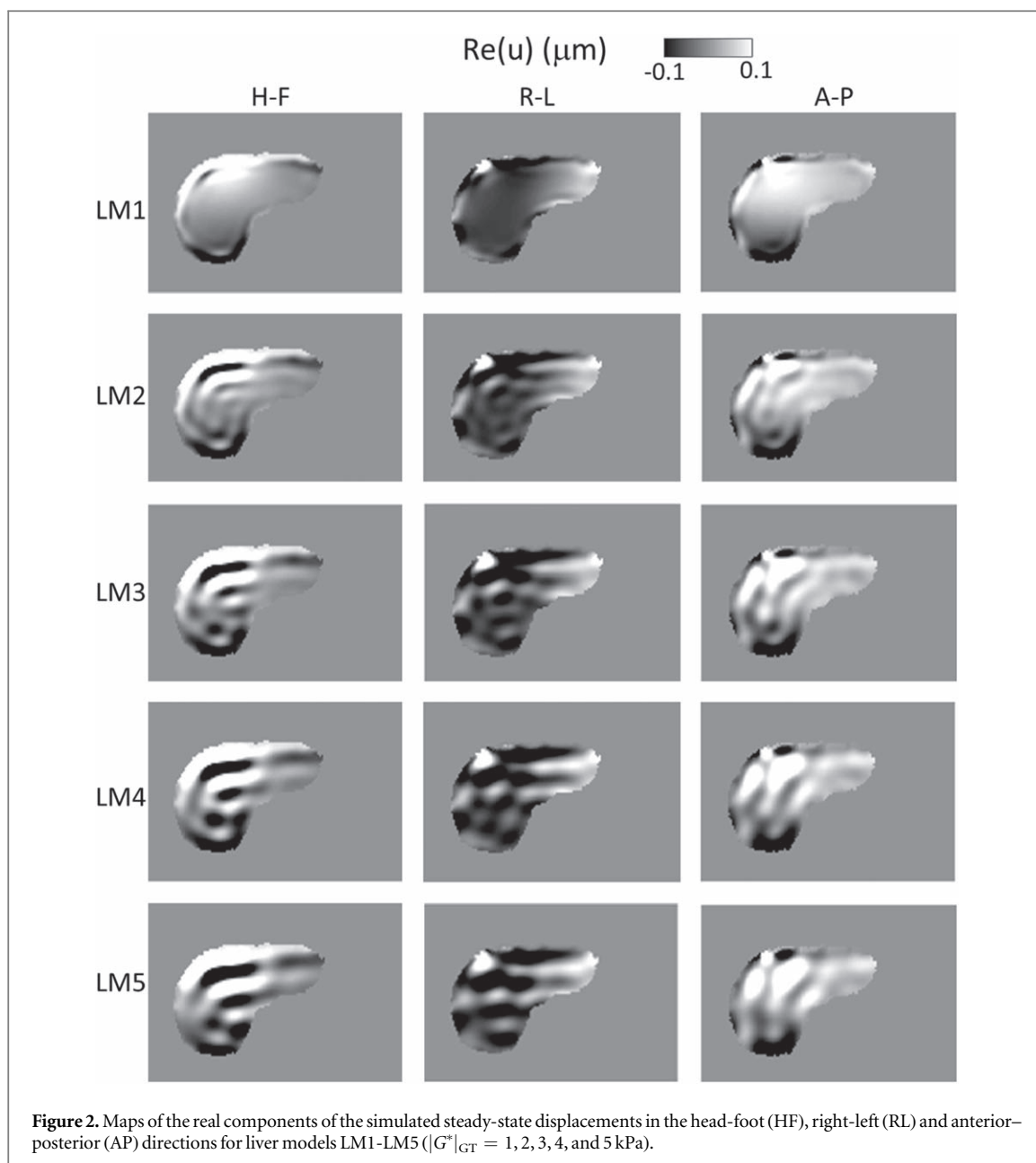
converted to shear waves when passing through the ribs before reaching the liver, with some wave-energy also reflected off the spine into the liver.

The sub-regions were defined by a combination of manual and automated segmentation of the mDixon scan. The outer edges of the model were selected manually from the water-only images, and for computational efficiency the model excluded the arms and was truncated at the neck and waist. Liver and bone regions were manually segmented using the water-only images, while fat was segmented automatically using signal-thresholding on the fat-only images. Binary masks were generated for each sub-region. While the automated segmentation steps could be completed rapidly, the manual segmentation of the rib cage was the most costly in terms of time and took several hours to complete.

FE meshes were prepared using ISO2MESH software, an open-source mesh generation toolbox, that uses surface and volumetric meshing algorithms from the computational geometry algorithms library (CGAL, www.cgal.org) (Tran *et al* 2020) and Tetgen (wias-berlin.de/software/tetgen). A combined multi-label mask of the torso and liver was made and used to create a linear four-node tetrahedral element mesh using the 'vol2mesh' function of ISO2MESH, which meshes each labelled region as a distinct, closed surface, ensuring there are shared nodes at region interfaces. The total number of model elements was 5117 417, with 4501 646 in the liver sub-mesh. The maximum volume of the liver elements was set to 1 mm³, the average element edge-length for the liver sub-mesh was 1.5 mm, and for the outer torso mesh 6.5 mm. A higher mesh density was prescribed for the liver, compared to outside the liver, to allow generation of simulated voxel sizes in the range of interest (≥ 2 mm isotropic). The processing time for the torso FEM MRE simulation was ~ 7 h, with parallel use of 8 processors on a dual-quad core PC with 256 GB RAM. Separate testing of a smaller tissue model for which three FEMs were generated with 0.5, 1 and 2 mm³ element volumes, demonstrated that the mean |G*| converged for all three element volumes at 2 mm simulated isotropic voxel resolution.

Fat was distributed across the torso volume, and therefore was not suitable for the creation of sub-meshes. The bone structure of the rib cage would have required very fine meshing for accurate representation, and this would have placed a high computational requirement on the parts of the FEM outside liver, when here the priority was for simulation accuracy inside the liver. Instead, the material properties for bone and fat were ascribed to individual elements of the torso model by identifying the elements whose centroids fell within the volume for each tissue type, as defined by the binary masks. Generalised soft tissue properties were assigned to the remaining elements of the torso. The material properties for all tissues are shown in table 1. Those assigned to the liver were varied between five sets of liver materials (LM1-LM5) which were estimated from MRE literature for healthy and diseased liver (Asbach *et al* 2008, Venkatesh *et al* 2013), and the other properties were ascribed based on literature values, e.g. for bone the cortical bone properties of the spine (Lee *et al* 2000). The liver properties could also have been estimated from *ex vivo* tissue measurements to provide an alternative and objective evaluation; however *ex vivo* measurements would not have allowed for the influence of blood pressure and the surrounding tissue matrix. All materials except bone were modelled as viscoelastic, while bone was modelled as linear elastic. Furthermore, all materials except bone were modelled as near-incompressible with hybrid elements (linear pressure) elements, in order to avoid volumetric locking by discretizing and solving for the pressure field independently of the displacements.

For the boundary conditions (BCs) (figure 1(b)) nodes were selected at the neck, shoulders and waist, and were fixed. These BCs achieved the dual purpose of tethering the model in space, and also had the benefit of reducing wave reflections from surfaces where the model was truncated, i.e. in reality waves would be free to pass through to the head, arms, abdomen and legs. Loading nodes (figure 1(c)) were selected on the model surface at a position corresponding to that used, and which is recommended, for liver MRE acquisitions, i.e. at the front of the body, over the lower ribs and to the right of the sternal notch (Quantitative Imaging Biomarkers



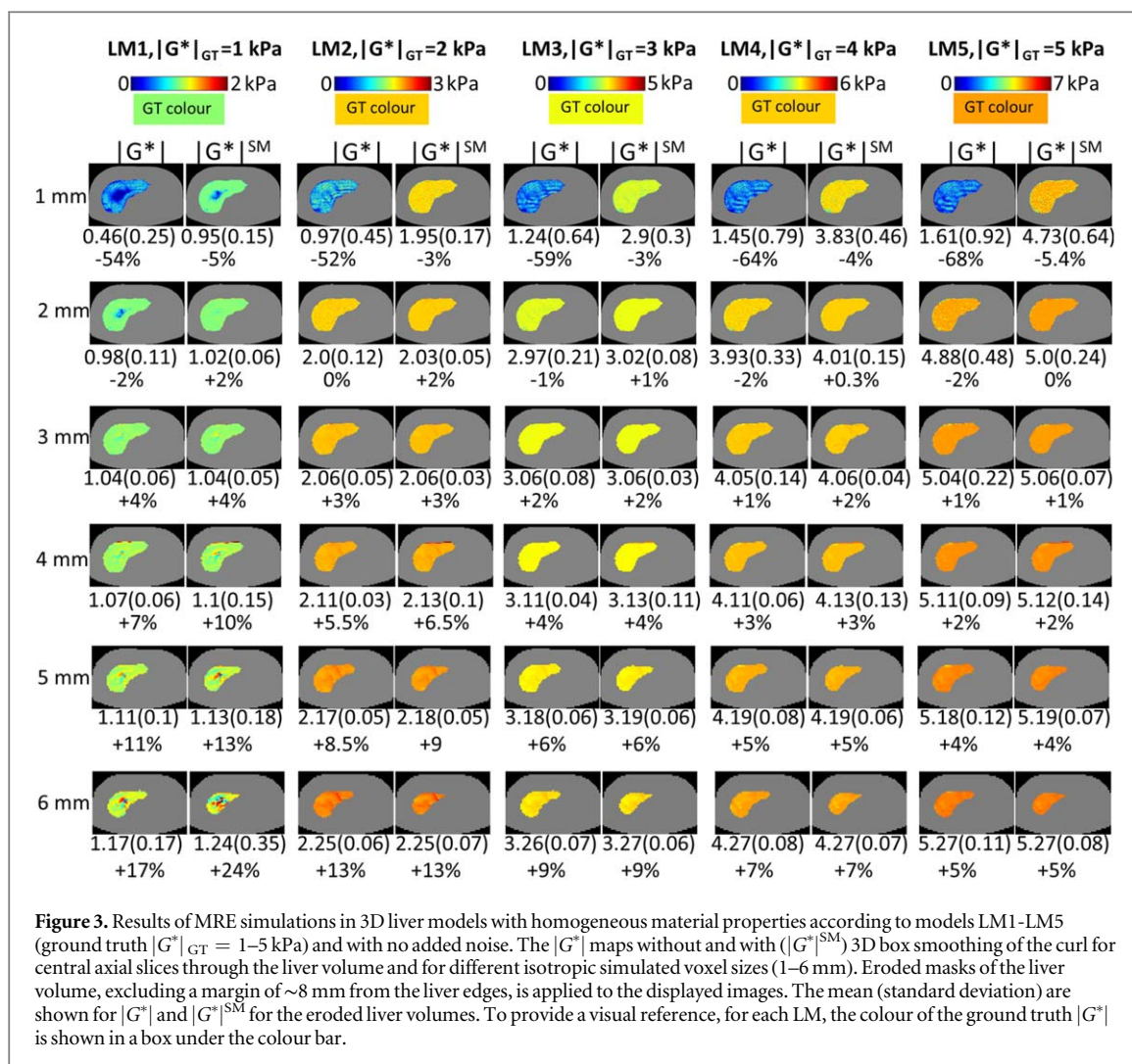
Alliance, 2018). MRE was simulated by delivering a harmonic displacement to the loading nodes at $30 \mu\text{m}$ amplitude and 60 Hz frequency in the anterior–posterior direction.

The nodal displacements were interpolated onto an isotropic ‘virtual-voxel’ grid with a step-size of 1 mm, using the MATLAB implementation of the ‘Natural Neighbour’ interpolation algorithm (Sibson 1981). The data was resampled to different isotropic resolutions by averaging the 1 mm data over varying cubic volumes to simulate the imaging partial-volume effect. Virtual phase-offset images ($N_{PO} = 8$) were calculated by multiplying the interpolated steady-state $\mathbf{u}(x)$ (equation (1)) by $\exp(i\alpha)$, and selecting the real component. Gaussian noise was added for the specified MM-SNR from the range 1–10 000, and the steady-state displacements recalculated by DFT.

3. Results

3.1. Simulated MRE motion data with no added noise

The real components of the simulated displacement fields in the H-F, R-L and A-P directions for LM1-LM5 are shown in figure 2. The wave patterns differ considerably with LM. For LM1 (ground truth $|G^*|_{GT} = 1 \text{ kPa}$, i.e. healthy liver) the waves are attenuated before reaching the liver centre. At higher $|G^*|_{GT}$ (moving to LM5), the waves travel further into the liver, and are reflected from the far boundary, resulting in interference patterns. For

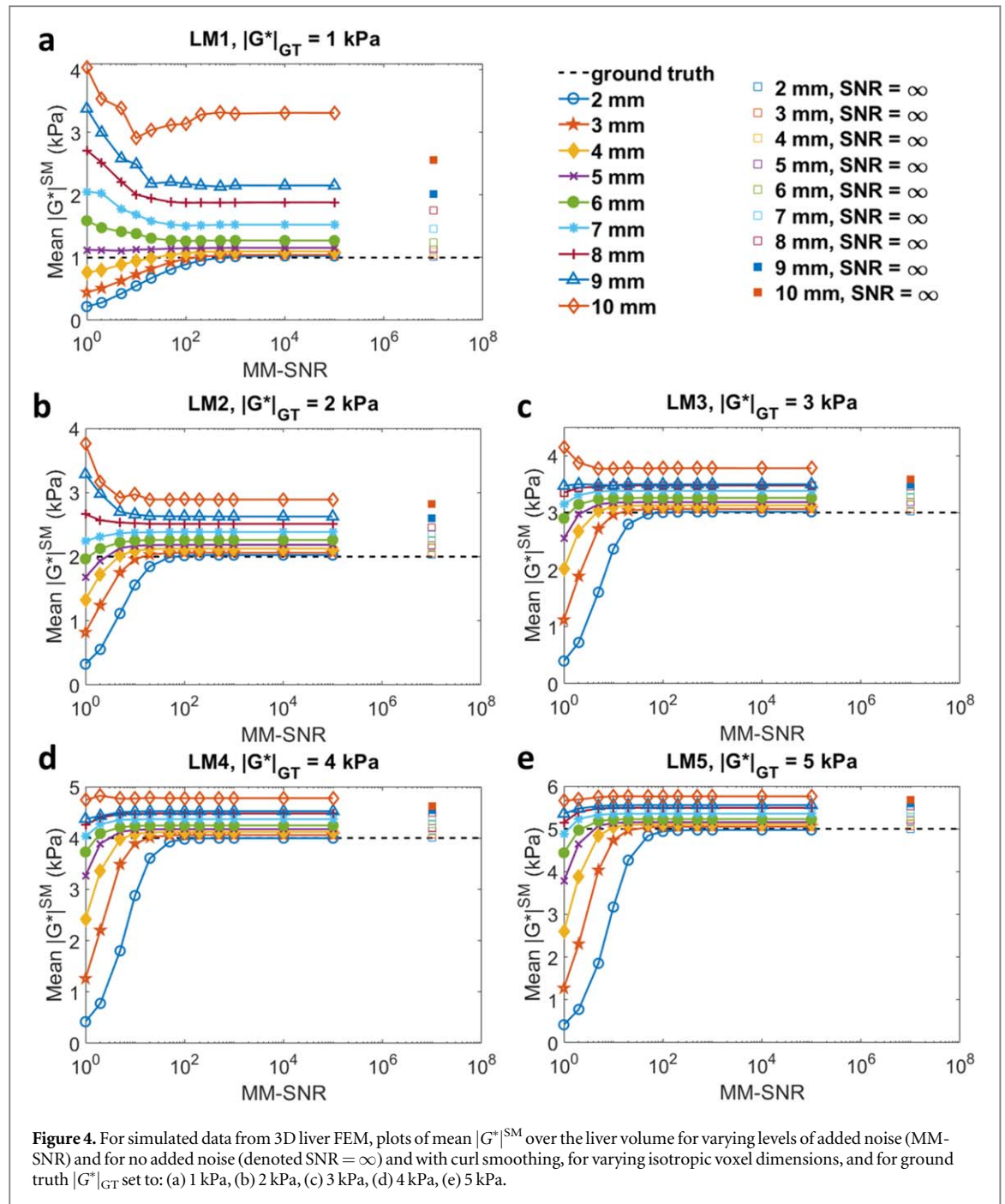


a given LM, the displacements in the three directions are of comparable amplitudes, with unpredictable patterns, especially for the A-P and R-L directions. See supporting information videos S1-S9 for animations of the simulated motion for LM2.

3.2. Effect of imaging resolution on simulated MRE accuracy with no added noise

Figure 3 shows simulated elastograms with no added noise for LM1-LM5 and isotropic voxel dimensions 1–6 mm, with the mean and SD, and percentage error on the mean compared with ground truth. For display and subsequent analysis the 3D mask of the liver volume was eroded by a margin of ~ 8 mm to exclude edge values which result from errors in the direct inversion near the interface of the liver with surrounding tissue (i.e. due to the assumption of local homogeneity in direct inversion and the complexity of the wave field at the boundaries where transmitted, reflected, and refracted waves are combined). Elastograms are compared without smoothing ($|G^*|$) and with ($|G^*|^{SM}$) 3D box filter smoothing of the curl. The focus is on the smoothed results, as the errors from simulation (even without added noise) warrant smoothing. For all LM the mean $|G^*|^{SM}$ values closest to the ground truth are at 2 mm resolution, with errors on the mean as low as 0% for LM5. In theory the results at 1 mm resolution for the 3D liver should exceed the accuracy of 2 mm. However as the average element edge-length for the 3D liver mesh was 1.5 mm, there was insufficient nodal density in the mesh to provide optimum results at 1 mm voxel size.

In general the elastograms are smooth at higher spatial resolutions (e.g. 2 mm), while at coarser resolutions artefactual patterns appear due to under-sampling of the complicated wave fields, as seen in 2D brain tissue simulations in McGrath *et al* (2016). Also, similarly to the data in McGrath *et al* (2016), there is a directly proportional overestimate of mean $|G^*|$ as the voxel size increases. In figure 3, at 2 mm resolution, for higher ground truth $|G^*|$ (e.g. $|G^*|_{GT} = 5$ kPa) the error artefacts are less prevalent compared to lower $|G^*|_{GT}$ (i.e. 1 and 2 kPa), and as the voxel size increases the artefacts are more accentuated for the low $|G^*|_{GT}$ simulations. For LM1, $|G^*|$ is overestimated in the centre of the liver as the wave amplitude has been attenuated to near zero, and the apparently long wavelengths are reconstructed as stiffer material.



3.3. Effect of added noise and imaging resolution on simulated MRE accuracy

Figure 4 plots the mean $|G^*|^{SM}$ for the eroded liver volumes versus levels of added noise (MM-SNR) for different resolutions and for LM1-LM5. The relationship between inversion accuracy, noise and resolution is complicated. In general, increased MM-SNR led to more accurate estimates of $|G^*|$. However, for larger voxel sizes $|G^*|$ was overestimated, as is the case for no added noise (figure 3). For lower MM-SNR, larger voxel sizes are needed to recover $|G^*|$, and the optimum voxel sizes increase with $|G^*|$.

Figure 5 plots the mean $|G^*|^{SM}$ over the (eroded) liver volume against the ground truth values for the different voxel sizes for the instance of no added noise and added noise with MM-SNR = 1, 2, 5, 10 and 20. Table 2 provides the optimum voxel size for each liver material LM1-LM5 and for all LMs combined for varying MM-SNR. As an example, if MM-SNR ≤ 5 and one wants to focus on the distinguishing between liver tissue of 2 and 3 kPa (i.e. early-stage liver fibrosis) then the optimum isotropic voxel size would be 4–6 mm.

3.4. Comparison of simulated and acquired liver MRE at matched imaging resolutions and MA-SNR

Matching resolutions and motion-SNR levels were compared between acquisitions and simulations, allowing assessment of acquired-elastogram accuracy.

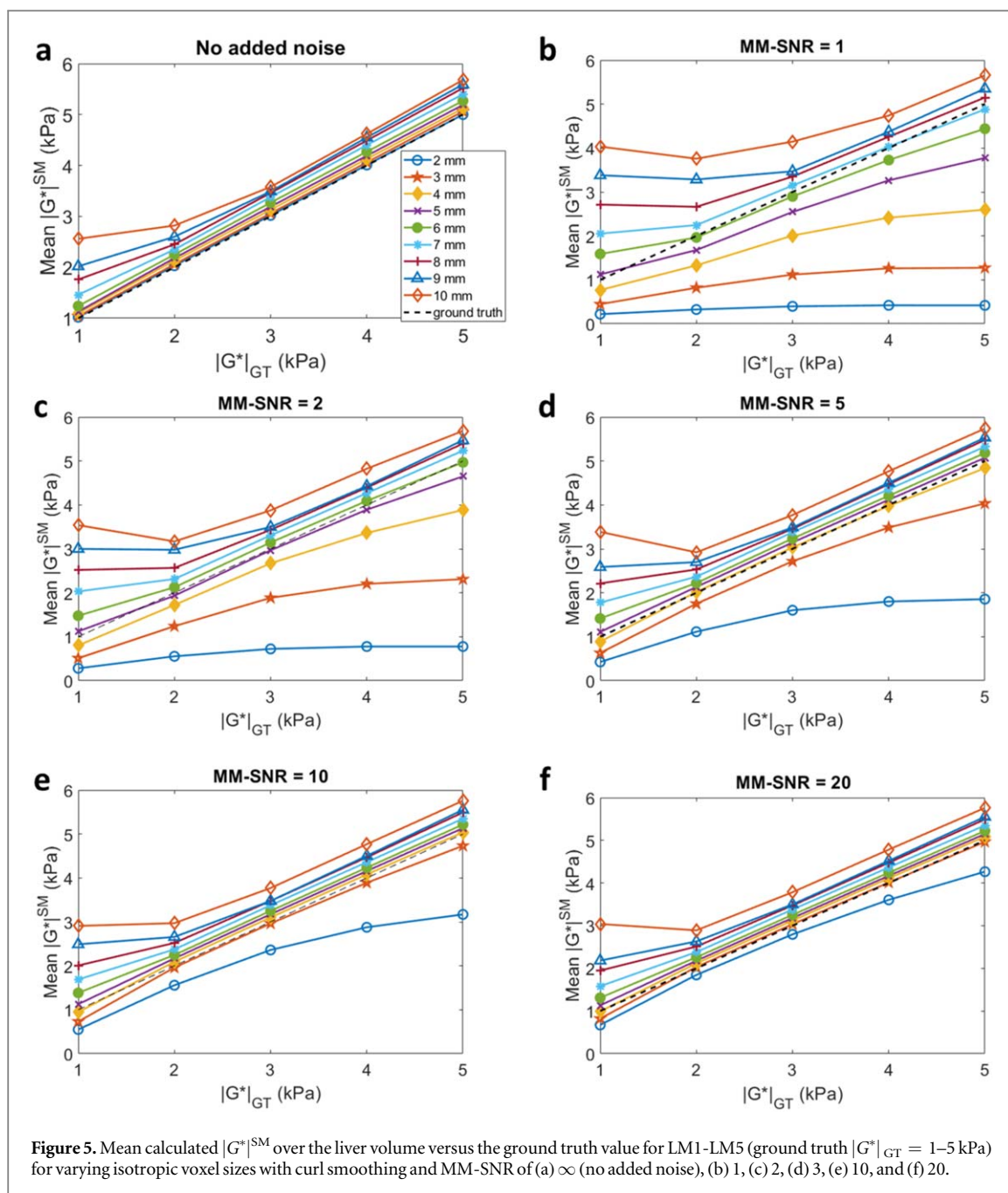
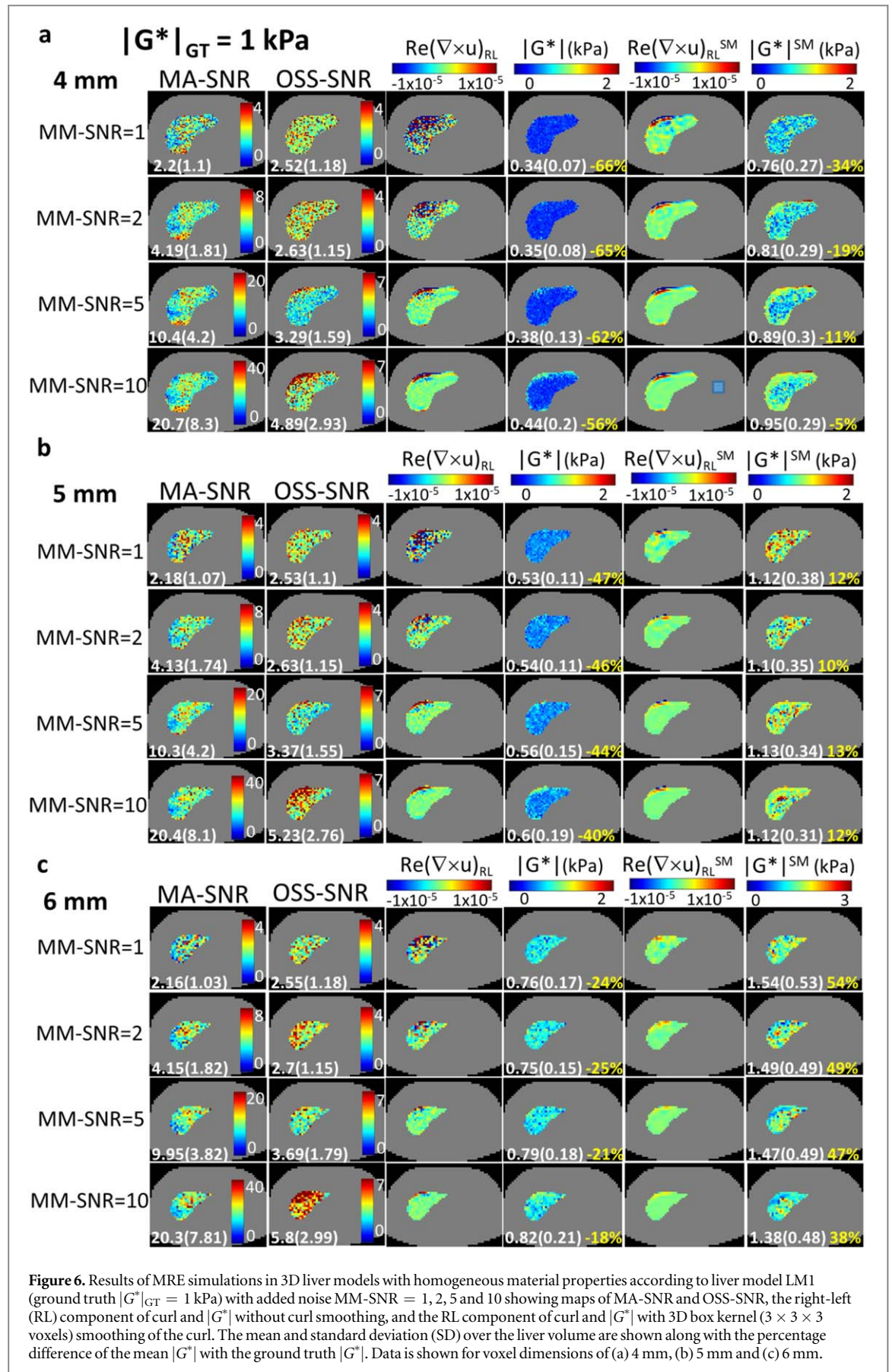


Figure 5. Mean calculated $|G^*|^{SM}$ over the liver volume versus the ground truth value for LM1-LM5 (ground truth $|G^*|_{GT} = 1-5$ kPa) for varying isotropic voxel sizes with curl smoothing and MM-SNR of (a) ∞ (no added noise), (b) 1, (c) 2, (d) 3, (e) 10, and (f) 20.

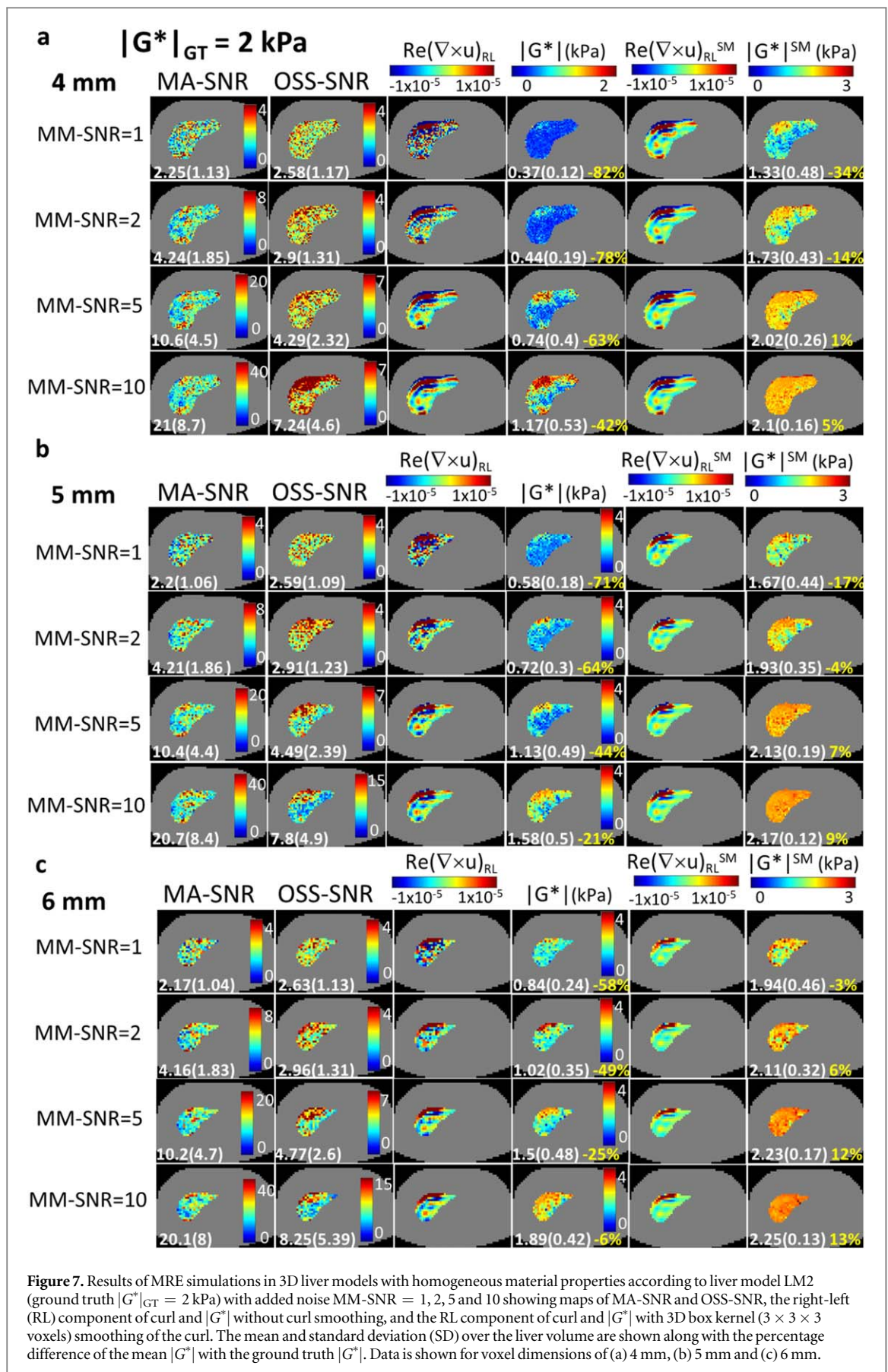
Table 2. Isotropic voxel dimensions to minimise the error in mean $|G^*|^{SM}$ for liver MRE.

Isotropic voxel dimensions to minimise the error in mean $ G^* ^{SM}$ for liver MRE (mm)						
MM-SNR	1	2	5	10	20	∞ (No added noise)
$ G^* _{GT}$ (kPa)						
1	5	5	5	4	4	2
2	6	5	4	3	3	2
3	6	5	4	3	3	2
4	7	6	4	4	3	2
5	7	6	5	4	3	2
Voxel dimension to minimise root mean square error for all $ G^* _{GT}$	6	5	4	4	3	2

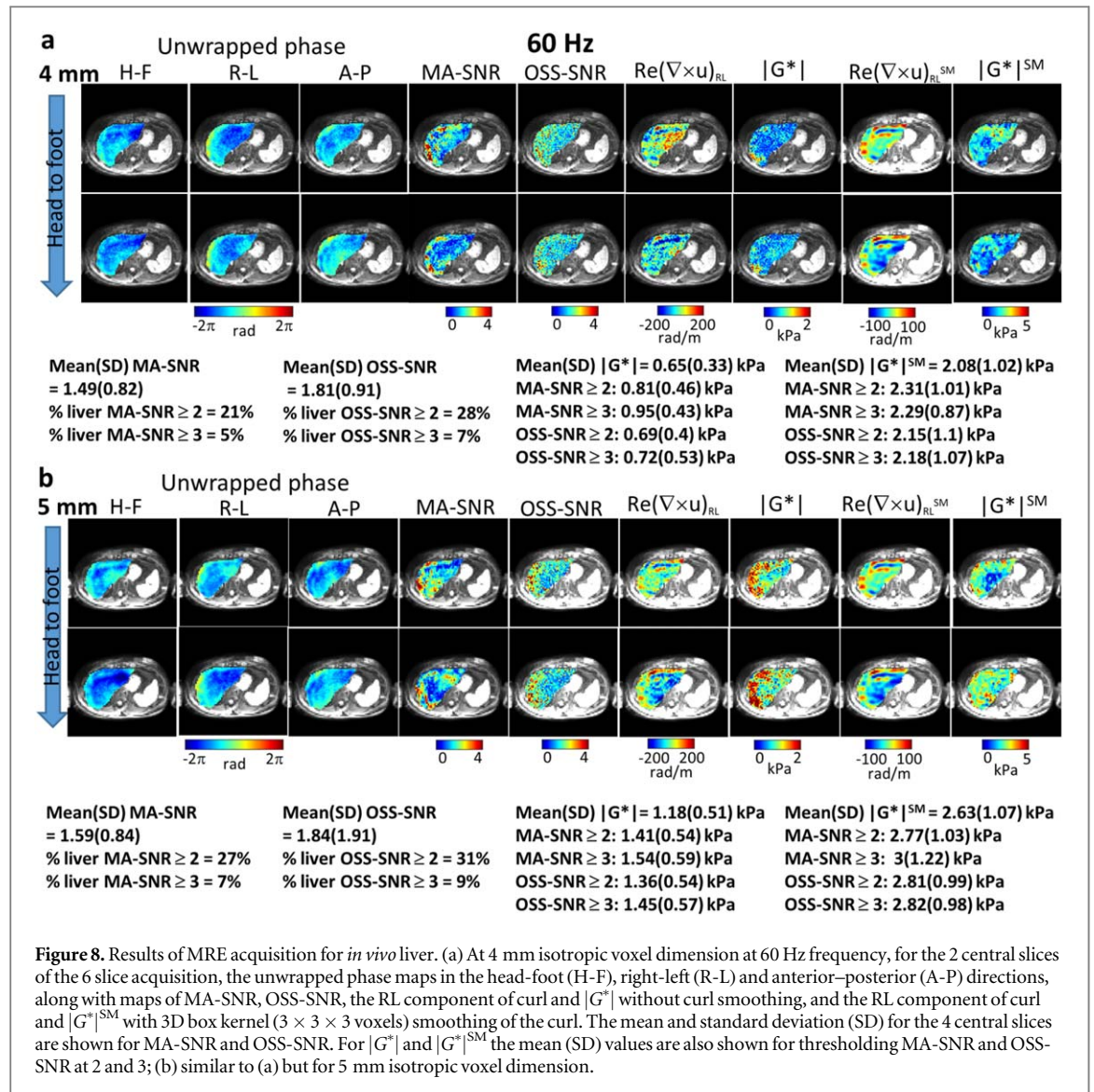
Figure 6 presents simulated results at 4, 5 and 6 mm resolution with MM-SNR of 1, 2, 5 and 10 for LM1, and figure 7 presents the equivalent for LM2. LM1 and LM2 were chosen as healthy liver is thought to have $|G^*|$ in the range of 1–2 kPa (Asbach et al 2008). The mean and SDs in $|G^*|$ are shown along with the percentage error of the mean compared with ground truth, and the errors vary greatly with MM-SNR and resolution, and between applying smoothing or not.



In figures 8 and 9, for the central 2 slices of the acquired 6 slices, the unwrapped phase, MA-SNR and OSS-SNR maps, and the curl and $|G^*|$ maps are shown without and with smoothing respectively. Figure 8 shows data at 4 and 5 mm at 60 Hz frequency, and figure 9 shows data at 6 mm for 50 and 60 Hz frequency.



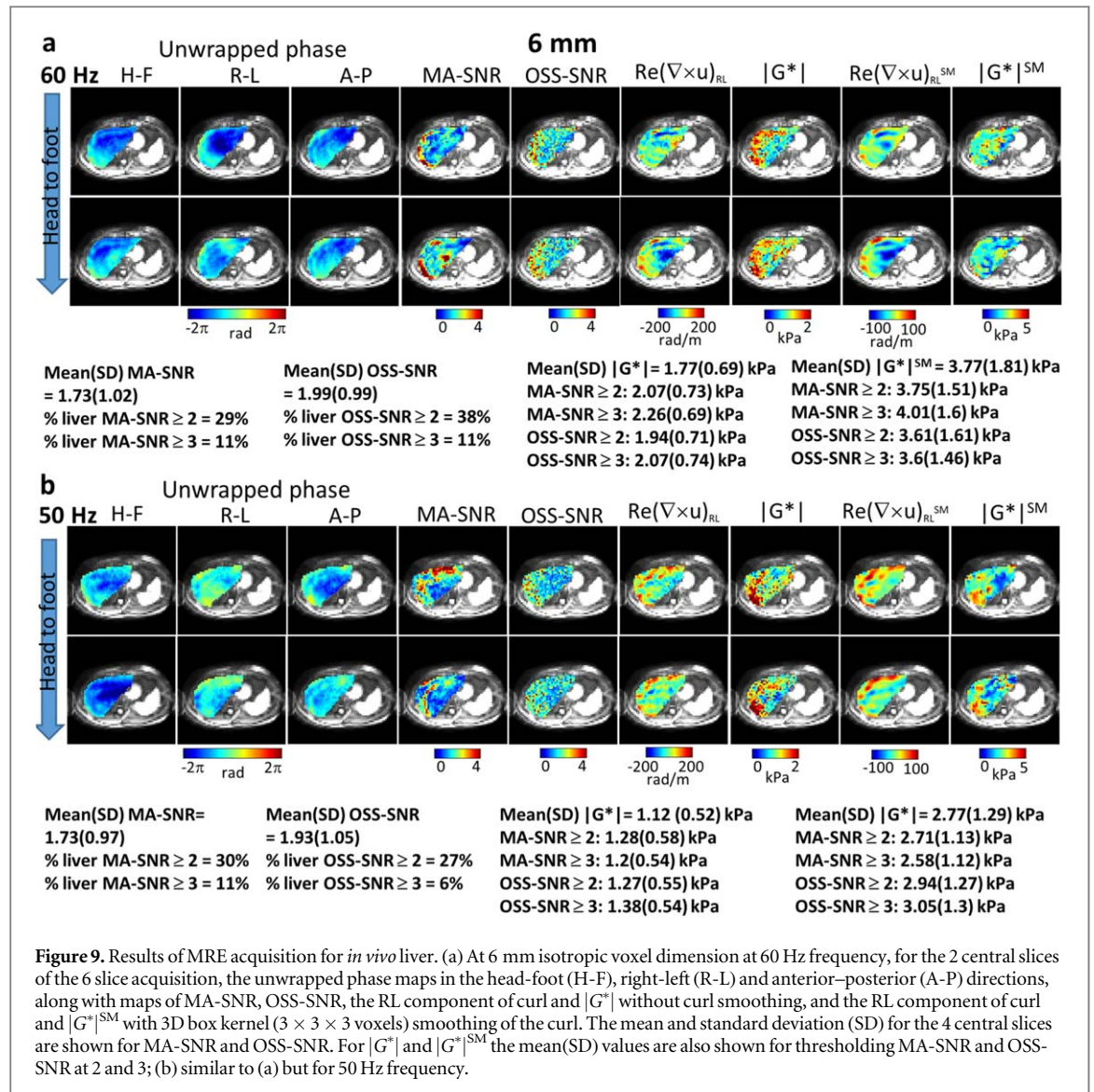
The mean MA-SNR values of the acquired data are quite low and increase slightly with voxel size, i.e. at 60 Hz, MA-SNR increases from 1.49 to 1.59 and 1.73 from 4 to 5 and 6 mm respectively. This is mainly driven by an increase in imaging-SNR with larger voxel size, but it does not increase linearly with voxel volume as the



harmonic motion estimates will be affected by loss of spatial resolution. Decreasing the frequency to 50 Hz resulted in no change in MA-SNR. In viscoelastic liver the motion field will vary with frequency, but also the imaging-SNR will change with altered acquisition parameters. Mean OSS-SNR also varies slightly: at 60 Hz OSS-SNR has a mean value of 1.81 at 4 mm and 1.84 at 5 mm, and at 6 mm this increases to 1.99, while at 50 Hz and 6 mm it decreases to 1.93. These changes are influenced by changing strain estimates over different imaging graphical prescriptions and frequency-dependent motion fields, in combination with varying noise contributions to the imaging signal.

For the acquired data, the mean $|G^*|$ at 60 Hz with no smoothing increases with voxel size from 0.65 to 1.18 and 1.77 kPa, and at 50 Hz it is reduced to 1.12 kPa. With smoothing the equivalent values are 2–3 times higher: 2.08, 2.63, 3.77 and 2.77 kPa. By creating masks based on thresholds of 2 and 3 in MA-SNR and OSS-SNR it was found that the mean $|G^*|$ tended to increase with the threshold.

Based on the MA-SNR values in the acquired data, it could be determined that the simulations with MM-SNR = 1 and 2 were the nearest equivalent (i.e. with $N_{\text{PO}} = 8$ MA-SNR is approximately 2 and 4). For LM1 at MM-SNR = 1 and 2, the most accurate mean $|G^*|$ values were at 5 mm with smoothing, i.e. 10% and 12% error (figure 6(b)). For LM2 at MM-SNR = 1 the most accurate mean $|G^*|$ was at 6 mm with smoothing, i.e. -3% (figure 7(c)), and at MM-SNR = 2 the best was at 5 mm with smoothing, i.e. -4% (figure 7(b)). As the $|G^*|$ values of the LM1 simulation are greatly biased by errors from the attenuated wave amplitude in the centre of the liver, and a similar degree of attenuation does not appear to occur in the acquisitions at 50 or 60 Hz, the LM2 simulation is seemingly a closer comparison to the acquired data. On that basis it could be deemed that for MM-SNR = 1–2 (MA-SNR = 2–4) the more reliable acquired elastograms are at 5 and 6 mm with smoothing, resulting in the mean $|G^*|$ for the acquired liver being estimated in the range of 2.63 and 3.77 kPa. However, also



of note is that at 5 and 6 mm (with smoothing) the errors for 1 kPa ground truth could be as high as 54% at 6 mm (figure 6(c)), and for a 2 kPa ground truth the absolute value of the error as high as 17% at 5 mm (figure 7(b)).

3.5. LFE inversion comparison

Supplementary figure S1 (available online at stacks.iop.org/PMB/66/225005/mmedia) shows the LFE elastograms with and without Gaussian band pass filtering for the acquired MRE data. Mean values over the slice with filtering are comparable with those for the direct inversion results with smoothing.

Supplementary figures S2 and S3 show results for the simulated data (with no added noise) without and with filtering respectively. It can be seen that only certain areas of the liver have values close to the ground truth (i.e. those areas closer to the point of wave delivery) and the results vary with liver tissue model (LM) and resolution. However, as this was an initial test with LFE, exploration of the optimisation of the algorithm with this simulated data was not carried out, and should be the subject of future investigations.

4. Discussion

4.1. The influence of imaging resolution on MRE accuracy

When no noise is added, one would expect flat simulated elastograms for uniform ground truth properties. However, simulated elastograms with no added noise had an artefact pattern, especially for LM1, where the displacement amplitudes were low at the liver centre, and smoothing accentuated this effect. These artefacts arise from a combination of error sources: (1) limited accuracy, which is a function of the FE mesh resolution and interpolation; (2) errors introduced to direct inversion when the voxel dimension is insufficiently small to

sample the wave field, particularly when the wavelength is short, or when the motion has a complicated pattern due to wave interference. In McGrath *et al* (2016) it was shown that with an appropriately small voxel size these errors can be reduced or eliminated. Indeed, in this study, for $|G^*|_{GT} \geq 2$ kPa at resolutions 2–4 mm the simulated liver elastograms were approximately uniform; while as the voxel size increased artefactual patterns emerged.

Other workers using 2D models and 3D geometric phantoms have made similar observations to this study with regard to optimum resolutions for given underlying properties and noise levels (Papazoglou *et al* 2008, Honarvar *et al* 2017, Yue *et al* 2017). The reason behind the dependence on imaging resolution is bound up with the finite difference calculation of the derivatives for the curl and Laplacian on a wave field. Aliasing of the waveforms occurs at insufficient sampling resolutions, and (when no noise is added) this results in over-estimates of $|G^*|$. At high resolutions (and no added noise) exact ground truth values can be recovered. When noise is added at high resolution this tends to cause underestimates of $|G^*|$, as the noise creates the impression of shorter wavelengths. Increasing the finite difference step-size can offset the influence of noise, as shown in Papazoglou *et al* (2008), Honarvar *et al* (2017), Yue *et al* (2017). At larger steps-size the gradient and therefore derivative values are greater, and hence the influence of noise becomes proportionately less.

The simulated motion fields indicate MRE waves travel into the liver from different directions, i.e. waves scattered from the ribs and reflected from the spine, and these may combine to form interference patterns in the liver centre. What was additionally identified in this study is these interference patterns can have effectively shorter wavelengths than the surrounding tissue, and hence the effect of under-sampling can be more pronounced in certain areas leading to an artefact pattern in the elastogram.

However, it is likely that wave attenuation and scattering in the real liver tissue would reduce the influence of reflected waves, and often pre-processing such as directional filtering is employed to reduce errors from reflections (Manduca *et al* 2003).

When noise was added to the simulated reflections of this study, different artefact patterns appeared in the elastograms, which were a combination of motion-noise and under-sampling of the wave field. In agreement with the findings of others (Papazoglou *et al* 2008, Honarvar *et al* 2017, Yue *et al* 2017), lower sampling resolutions could offset the influence of noise on the mean $|G^*|$, and for a given scenario of noise, underlying material properties, anatomy and wave delivery, a finite optimum imaging resolution could be identified. However, lower sampling resolutions can also increase the errors of direct inversion due to poorer estimates of the derivatives.

In Yue *et al* (2017) it was identified that for direct inversion with finite differences the number of voxels per shear wavelength should be ≥ 8.3 . In Hu (2020) direct inversion was compared with LFE, and it was found that direct inversion required ≥ 10 voxels per wavelength, compared to a limit of 2 for LFE. The shear wavelengths for LM1-LM5 of this study are 13, 23, 28, 33 and 37 mm. Hence at 1 mm resolution the wavefields for all tissue models should be sufficiently resolved, provided that wave interference does not result in effectively shorter wavelengths in portions of the images. At 2 mm resolution the wavefields of LM2-LM5 should still be sufficiently resolved.

The findings of this study highlight how critical spatial resolution is to MRE accuracy. The choice of MRI voxel dimension is a trade-off between preserving spatial resolution or SNR. Liver MRE is often carried out using non-isotropic imaging resolutions, e.g. $4.7 \times 4.9 \times 10$ mm³ (Quantitative Imaging Biomarkers Alliance 2018), but more recent work has moved to isotropic graphical prescriptions which are suited to 3D inversion (Guo *et al* 2014, Sinkus *et al* 2018). For methods that measure one (through-plane) motion direction and solve for a 2D slice, such as the one-motion-direction implementation of Multi-model direct inversion (Yoshimitsu *et al* 2017), data is often acquired for larger voxels and reconstructed by the scanner to a higher resolution in-plane. Polynomial fits are used to estimate derivatives, and hence the noise and resolution issues identified here are obviated.

The acquisition voxel dimensions employed in this study (4, 5 and 6 mm) were chosen based on the simulation results for healthy liver (LM1-LM2) and low MA-SNR (< 10). Although previous work has highlighted the relationship of accuracy to both resolution and noise in more simplistic geometries (Papazoglou *et al* 2008, Honarvar *et al* 2017, Yue *et al* 2017), unique in this work is that predictions have been made based on an anthropomorphic personalised liver model, which is matched to the MRE acquisition, allowing a fuller evaluation of liver MRE accuracy. Comparison of the MRE acquisition with simulations at matching resolutions and MA-SNR levels indicated which resolutions are likely to have yielded elastograms closest to the true underlying properties, and also what the magnitude of error might be in the acquired elastograms. Therefore this study indicates that MRE imaging resolution must be chosen carefully based on the expected range of $|G^*|$. However, even when an optimum resolution has been identified, possible errors on the order of 54% ($|G^*|_{GT} = 1$ kPa, 6 mm, with smoothing) exist. In liver disease, $|G^*|$ will increase with the progressive stages of fibrosis, but can vary by < 1 kPa between stages (Venkatesh *et al* 2013). Errors of this magnitude could be critical in distinguishing healthy and diseased liver, and the fibrosis stages. However, it is likely that the error magnitudes

predicted by this study exceed those in practice, due to the simplicity of the simulation, pre-processing and direct inversion approach employed, which amplifies the influence of noise through derivative calculation.

The artefacts in the simulated elastograms have a structure which could be misinterpreted as true variations with disease or anatomy (i.e. the vascular tree). In the acquired MRE elastograms there is a structured variation in $|G^*|$, which may indeed be associated with liver anatomy, or might be influenced by under-sampling of the wave field.

Partial-volume errors occur at the liver boundaries for the simulated and acquired data. Additionally, more complicated motion fields will occur at the tissue interfaces, as waves are scattered and refracted due to acoustic impedance mismatch, which when under-sampled can cause elastogram errors (McGrath *et al* 2016). Coupled with this is the inherent assumption of local-homogeneity in direct inversion, which causes errors at the boundaries of tissues with different properties (McGrath *et al* 2016). The liver $|G^*|$ variations in the acquired elastograms might be artefacts resulting from the assumption of local homogeneity, or indeed the further assumption of isotropy. Recent work has developed algorithms avoiding these assumptions (Barnhill *et al* 2018, Fovargue *et al* 2018, Sinkus *et al* 2000). However, any inversion algorithm is likely to be hampered by insufficient spatial-sampling of the displacements. Hence, these observations indicate that methodological improvements should be pursued to increase resolution, e.g. by reducing echo time through use of higher harmonic frequency MEGs (Herzka *et al* 2009) and leveraging the increased SNR to obtain higher resolution data. Alternatively, imaging during free-breathing or applying retrospective gating (as opposed to imaging during breath-hold) would allow higher resolutions while preserving SNR (Tzschätzsch *et al* 2016), through collecting multiple signal averages or phase offsets. Another approach to offset the effect of undersampling is to use interpolation (Yue *et al* 2017), but this employs assumptions of the local homogeneity of the tissue biomechanics. Methods such as the multi-model direct inversion (Yoshimitsu *et al* 2017) employ polynomial fitting for derivative calculation, which can also offset problems with under sampling and noise.

Other studies on MRE validation have identified important factors which determine MRE accuracy. For example in Tweten *et al* (2017) it was found that with respect to identifying anisotropic material properties, multiple slow and fast shear waves with different propagation directions should be present, and directional filter inversion with LFE was compared with curl-based methods.

4.2. Motion-based and strain-based SNR for evaluation of MRE accuracy

By applying MA-SNR and OSS-SNR threshold-masks, different mean $|G^*|$ values were obtained, which tended to increase with threshold. This is a similar approach to methods such as multi-scale and multi-model direct inversion which incorporate cross-hatching on the elastograms representing 95% confidence thresholds on model fitting (Yoshimitsu *et al* 2017).

MRE-measured motion depends on the phase accrual of the tissue moving in the MEG, which can be improved by: (1) increasing MEG amplitude; (2) more efficient wave delivery; (3) frequency-optimisation to reduce wave attenuation in viscoelastic tissue. Higher MA-SNR could also be achieved by increasing imaging-SNR, increasing N_{PO} (e.g. by using free-breathing) or reducing TE (e.g. by using MEGs at higher harmonic frequencies).

Changing imaging resolution resulted in slight variations in MA-SNR and OSS-SNR, which were driven by a combination of factors. Although imaging-noise is reduced in larger voxels, the displacement and strain measures will also vary with resolution. These initial observations indicate that voxel-wise MA-SNR and OSS-SNR could be used to guide the choice of MRE acquisition parameters and as a metric for summary-statistic preparation.

4.3. Comparison with LFE

The initial evaluation of LFE demonstrated that similar results could be obtained for the acquired data when using LFE with filtering, compared with the direct inversion with smoothing. However for the simulated data only portions of the liver slice elastograms had values close to ground truth. In Hu (2020) LFE and direct inversion were shown to produce different results dependent on frequency and resolution. Future studies will carry out a fuller investigation and optimisation of LFE.

4.4. Study limitations

Limitations of this study are: (1) only one personalised FEM was generated; (2) homogeneous material properties were prescribed for the simulated liver; (3) Other anatomical aspects were not considered in the simulation, such as the organ capsule, pulsations from blood vessels, variations in fat and muscle or fluid (i.e. ascites), or aspects of liver disease such as atrophy; (4) the MRE driver position was not varied; (5) more advanced methods of noise reduction such as in Barnhill *et al* (2017) were not explored; (6) likewise methods of reducing the effects of reflection and interference were not applied such as in Manduca *et al* (2003). The direct

inversion method has assumptions of isotropy and local homogeneity, and involves calculation of third order derivatives, which amplifies imaging-noise. Future work will use this methodology to incorporate: (1) a range of FEM models generated from patients and volunteers; (2) variations in liver properties with anatomy and disease, heterogeneity and anisotropy; (3) comparison of repeat MRE acquisitions at different driver positions; (4) comparison with other inversion methods, which may be less sensitive to spatial resolution and noise, and pre-processing methods to reduce the influence of noise and reflections.

5. Conclusion

This simulation study has demonstrated important considerations for the optimisation of liver MRE. A range of factors were found to greatly impact MRE results: (1) imaging resolution; (2) data smoothing during inversion, (3) MA-SNR and OSS-SNR threshold. The simulated liver elastogram error was dependent on ground truth properties in combination with imaging resolution and motion-SNR, suggesting that liver MRE should be planned according to the expected liver $|G^*|$. For example, in healthy liver ($|G^*| = 2$ kPa) and an anticipated MA-SNR < 5 , the optimum imaging resolution is predicted to be 5–6 mm. To obtain greater accuracy for diseased liver ($|G^*| \geq 3$ kPa), an increase in voxel size should be considered.

It was determined that at typical voxel sizes the error on the mean $|G^*|$ could be on the order of 54% for healthy liver ($|G^*| = 1$ kPa) at 60 Hz; an uncertainty of 0.54 kPa. As liver $|G^*|$ can vary between stages of fibrosis by < 1 kPa, this consideration is vital in the development of liver MRE as a disease biomarker. However further work is required to fully explore and determine the limitations of these findings.

Acknowledgments

This work was supported by the Medical Research Council Grant [grant number MC_PC_16055]. Financial support was also received from the NIHR Biomedical Research Centre (NIHR BRC); Gastrointestinal and Liver Disorder theme, Nottingham University Hospitals NHS Trust and University of Nottingham. This article presents independent research funded and supported by the NIHR Nottingham Digestive Diseases Biomedical Research Unit, Nottingham University Hospitals NHS Trust and University of Nottingham. Views expressed are those of the authors and not necessarily those of the NHS, NIHR or Department of Health.

Ethical statement

The study was approved by the University of Nottingham Medical School Ethics Committee (Approval number: H1408201428). The scan on the one healthy subject was conducted in accordance with the principles embodied in the Declaration of Helsinki and in accordance with local statutory requirements.

CRediT author statement

Deirdre McGrath: Conceptualization, Methodology, Software, Formal analysis, Investigation, Writing-Original Draft and Revision, Visualization.

Christopher Bradley: Investigation, Writing-Review and Editing.

Susan Francis: Investigation, Writing-Review and Editing, Supervision, Project administration, Funding acquisition.

ORCID iDs

Deirdre M McGrath  <https://orcid.org/0000-0002-0823-8932>

Christopher R Bradley  <https://orcid.org/0000-0002-2174-2279>

Susan T Francis  <https://orcid.org/0000-0003-0903-7507>

References

- Asbach P, Klatt D, Hamhaber U, Braun J, Somasundaram R, Hamm B and Sack I 2008 Assessment of liver viscoelasticity using multifrequency MR elastography *Magn. Reson. Med.* **60** 373–9
- Barnhill E, Davies P J, Ariyurek C, Fehlner A, Braun J and Sack I 2018 Heterogeneous multifrequency direct inversion (HMEDI) for magnetic resonance elastography with application to a clinical brain exam *Med. Image Anal.* **46** 180–8

- Barnhill E, Hollis L, Sack I, Braun J, Hoskins P R, Pankaj P, Brown C, van Beek E J R and Roberts N 2017 Nonlinear multiscale regularisation in MR elastography: towards fine feature mapping *Med. Image Anal.* **35** 133–45
- Cunha G M, Glaser K J, Bergman A, Luz R P, de Figueiredo E H and Lobo Lopes F P P 2018 Feasibility and agreement of stiffness measurements using gradient-echo and spin-echo MR elastography sequences in unselected patients undergoing liver MRI *Br. J. Radiol.* **91** 1087
- Dittmann F, Hirsch S, Tzschatzsch H, Guo J, Braun J and Sack I 2016 *In vivo* wideband multifrequency MR elastography of the human brain and liver *Magn. Reson. Med.* **76** 1116–26
- Dixon W T 1984 Simple proton spectroscopic imaging *Radiology* **153** 189–94
- Doyley M M 2012 Model-based elastography: a survey of approaches to the inverse elasticity problem *Phys. Med. Biol.* **57** R35–73
- Fovargue D, Kozerke S, Sinkus R and Nordsletten D 2018 Robust MR elastography stiffness quantification using a localized divergence free finite element reconstruction *Med. Image Anal.* **44** 126–42
- Guo J, Hirsch S, Streitberger K J, Kamphues C, Asbach P, Braun J and Sack I 2014 Patient-activated three-dimensional multifrequency magnetic resonance elastography for high-resolution mechanical imaging of the liver and spleen *RoFo : Fortschr. auf dem Geb. Röntgenstrahlen und der Nuklearmedizin* **186** 260–6
- Herzka D A, Kotys M S, Sinkus R, Pettigrew R I and Gharib A M 2009 Magnetic resonance elastography in the liver at 3 Tesla using a second harmonic approach *Magn. Reson. Med.* **62** 284–91
- Honarvar M, Sahebjavaher R S, Rohling R and Salcudean S E 2017 A comparison of finite element-based inversion algorithms, local frequency estimation, and direct inversion approach used in MRE *IEEE Trans. Med. Imaging* **36** 1686–98
- Hu L 2020 Requirements for accurate estimation of shear modulus by magnetic resonance elastography: a computational comparative study *Comput. Methods Programs Biomed.* **192** 105437
- Kritsaneepaiiboon S, Ina N, Chotsampancharoen T, Roymanee S and Cheewatanakornkul S 2018 The relationship between myocardial and hepatic T_2 and T_2^* at 1.5T and 3T MRI in normal and iron-overloaded patients *Acta Radiol.* **59** (Stockholm, Sweden: Sage Publications) 355–62 (Stockholm, Sweden: 1987)
- Lee C K, Kim Y E, Lee C S, Hong Y M, Jung J M and Goel V K 2000 Impact response of the intervertebral disc in a finite-element model *Spine* **25** 2431–9
- Madsen E L, Hobson M A, Frank G R, Shi H, Jiang J, Hall T J, Varghese T, Doyley M M and Weaver J B 2006 Anthropomorphic breast phantoms for testing elastography systems *Ultrasound Med. Biol.* **32** 857–74
- Madsen E L, Kelly-Fry E and Frank G R 1988 Anthropomorphic phantoms for assessing systems used in ultrasound imaging of the compressed breast *Ultrasound Med. Biol.* **14** 183–201
- Manduca A, Lake D S, Kruse S A and Ehman R L 2003 Spatio-temporal directional filtering for improved inversion of MR elastography images *Med. Image Anal.* **7** 465–73
- Manduca A, Oliphant T E, Dresner M A, Mahowald J L, Kruse S A, Amromin E, Felmlee J P, Greenleaf J F and Ehman R L 2001 Magnetic resonance elastography: non-invasive mapping of tissue elasticity *Med. Image Anal.* **5** 237–54
- Mathew R P and Venkatesh S K 2018 Imaging of hepatic fibrosis *Curr. Gastroenterol. Rep.* **20** 45
- McGarry M D, Van Houten E E, Perrinez P R, Pattison A J, Weaver J B and Paulsen K D 2011 An octahedral shear strain-based measure of SNR for 3D MR elastography *Phys. Med. Biol.* **56** N153–64
- McGrath D M 2018 *Biomechanics of Soft Tissues: Principles and Applications* ed A Al Mayah (Boca Raton: CRC Press) pp 55–94
- McGrath D M, Foltz W D, Al-Mayah A, Niu C J and Brock K K 2012 Quasi-static magnetic resonance elastography at 7 T to measure the effect of pathology before and after fixation on tissue biomechanical properties *Magn. Reson. Med.* **68** 152–65
- McGrath D M, Ravikumar N, Beltrachini L, Wilkinson I D, Frangi A F and Taylor Z A 2017 Evaluation of wave delivery methodology for brain MRE: insights from computational simulations *Magn. Reson. Med.* **78** 341–56
- McGrath D M, Ravikumar R, Wilkinson I D, Frangi A F and Taylor Z 2016 Magnetic resonance elastography of the brain: an *in silico* study to determine the influence of cranial anatomy *Magn. Reson. Med.* **76** 645–62
- Morisaka H, Motosugi U, Ichikawa S, Nakazawa T, Kondo T, Funayama S, Matsuda M, Ichikawa T and Onishi H 2018 Magnetic resonance elastography is as accurate as liver biopsy for liver fibrosis staging *J. Magn. Reson. Imaging : JMRI* **47** 1268–75
- Murphy M C, Huston J 3rd, Jack C R Jr, Glaser K J, Senjem M L, Chen J, Manduca A, Felmlee J P and Ehman R L 2013 Measuring the characteristic topography of brain stiffness with magnetic resonance elastography *PLoS One* **8** e81668
- Muthupillai R, Lomas D J, Rossman P J, Greenleaf J F, Manduca A and Ehman R L 1995 Magnetic resonance elastography by direct visualization of propagating acoustic strain waves *Science* **269** 1854–7
- Muthupillai R, Rossman P J, Lomas D J, Greenleaf J F, Riederer S J and Ehman R L 1996 Magnetic resonance imaging of transverse acoustic strain waves *Magn. Reson. Med.* **36** 266–74
- Papazoglou S, Hamhaber U, Braun J and Sack I 2008 Algebraic helmholtz inversion in planar magnetic resonance elastography *Phys. Med. Biol.* **53** 3147–58
- Quantitative Imaging Biomarkers Alliance (QIBA) 2018 QIBA Profile: Magnetic Resonance Elastography of the Liver; Stage 2: Consensus Profile- <https://qibawiki.rsna.org/images/a/a5/MRE-QIBAProfile-2018-05-02-CONSENSUS.pdf>
- Sibson R 1981 *Interpreting Multivariate Data* ed B V Chichester (NJ, USA: John Wiley) pp 21–36978-0471280392
- Singh S et al 2015 Diagnostic performance of magnetic resonance elastography in staging liver fibrosis: a systematic review and meta-analysis of individual participant data *Clin. Gastroenterol. Hepatol.* **13** 440–51.e6
- Sinkus R, Lambert S, Abd-Elmoniem K Z, Morse C, Heller T, Guenther C, Ghanem A M, Holm S and Gharib A M 2018 Rheological determinants for simultaneous staging of hepatic fibrosis and inflammation in patients with chronic liver disease *NMR Biomed.* **31** e3956
- Sinkus R, Lorenzen J, Schrader D, Lorenzen M, Dargatz M and Holz D 2000 High-resolution tensor MR elastography for breast tumour detection *Phys. Med. Biol.* **45** 1649–64
- Sinkus R, Tanter M, Xydeas T, Catheline S, Bercoff J and Fink M 2005 Viscoelastic shear properties of *in vivo* breast lesions measured by MR elastography *Magn. Reson. Imaging* **23** 159–65
- Tran A P, Yan S and Fang Q 2020 Improving model-based functional near-infrared spectroscopy analysis using mesh-based anatomical and light-transport models *Neurophotonics* **7** 015008
- Tweten D J, Okamoto R J and Bayly P V 2017 Requirements for accurate estimation of anisotropic material parameters by magnetic resonance elastography: a computational study *Magn. Reson. Med.* **78** 2360–72
- Tzschätzsch H, Guo J, Dittmann F, Hirsch S, Barnhill E, Jöhrens K, Braun J and Sack I 2016 Tomoelastography by multifrequency wave number recovery from time-harmonic propagating shear waves *Med. Image Anal.* **30** 1–10
- Van Houten E E, Paulsen K D, Miga M I, Kennedy F E and Weaver J B 1999 An overlapping subzone technique for MR-based elastic property reconstruction *Magn. Reson. Med.* **42** 779–86

- Venkatesh S K, Yin M and Ehman R L 2013 Magnetic resonance elastography of liver: technique, analysis, and clinical applications *J. Magn. Reson. Imaging* **37** 544–55
- Xiang Q S 2006 Two-point water-fat imaging with partially-opposed-phase (POP) acquisition: an asymmetric Dixon method *Magn. Reson. Med.* **56** 572–84
- Yin M, Talwalkar J A, Glaser K J, Manduca A, Grimm R C, Rossman P J, Fidler J L and Ehman R L 2007 Assessment of hepatic fibrosis with magnetic resonance elastography *Clin. Gastroenterol. Hepatol.* **5** 1207–13
- Yoshimitsu K, Shinagawa Y, Mitsufuji T, Mutoh E, Urakawa H, Sakamoto K, Fujimitsu R and Takano K 2017 Preliminary comparison of multi-scale and multi-model direct inversion algorithms for 3T MR elastography *Magn. Reson. Med. Sci.* **16** 73–7
- Yue J L, Tardieu M, Julea F, Boucneau T, Sinkus R, Pellot-Barakat C and Maitre X 2017 Acquisition and reconstruction conditions *in silico* for accurate and precise magnetic resonance elastography *Phys. Med. Biol.* **62** 8655–70